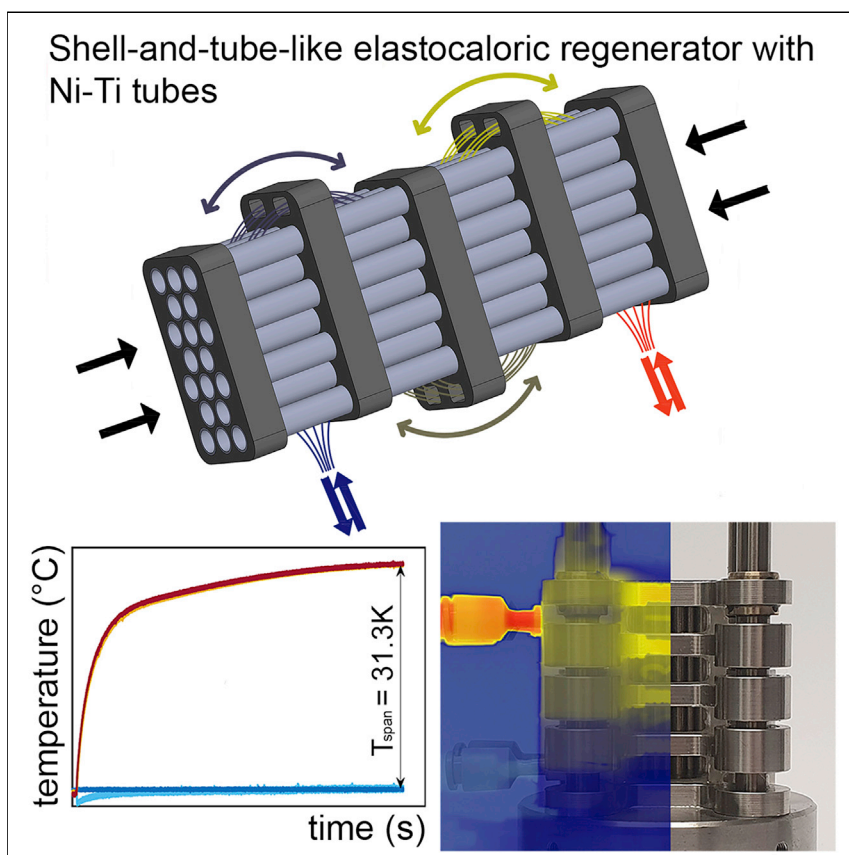


Article

# High-performance cooling and heat pumping based on fatigue-resistant elastocaloric effect in compression



Žiga Ahčin, Stefano Dall’Olio, Andrej Žerovnik, ..., Miha Brojan, Jernej Klemenc, Jaka Tušek

jaka.tusek@fs.uni-lj.si

Highlights

A shell-and-tube-like elastocaloric regenerator was developed and tested

Record performance with a temperature span of more than 31 K was achieved

Maximum specific cooling/heating powers of more than 4,400 W/kg were obtained

Over 300,000 cycles up to 825 MPa were performed without degradation or fatigue

Elastocaloric cooling shows considerable potential as an alternative to vapor-compression refrigeration, but fatigue-related problems limit its true potential. Here, we present a new design of an elastocaloric regenerator consisting of Ni–Ti tubes loaded in compression, acting as a cooling or heat-pumping device. It enables durable operation and record performance with a temperature span of more than 31 K (in heat-pumping mode) and heating/cooling powers above 60 W (equivalent to 4,400 W per kg of elastocaloric material).

Article

# High-performance cooling and heat pumping based on fatigue-resistant elastocaloric effect in compression

Žiga Ahčin,<sup>1</sup> Stefano Dall'Olio,<sup>1</sup> Andrej Žerovnik,<sup>1</sup> Urban Žvar Baškovič,<sup>1</sup> Luka Porenta,<sup>1</sup> Parham Kabirifar,<sup>1</sup> Jan Cerar,<sup>1</sup> Samo Zupan,<sup>1</sup> Miha Brojan,<sup>1</sup> Jernej Klemenc,<sup>1</sup> and Jaka Tušek<sup>1,2,\*</sup>

## SUMMARY

In recent years, elastocaloric cooling has shown great potential as an alternative to vapor-compression refrigeration. However, there is still no existing elastocaloric device that offers fatigue-resistant operation and yet high cooling/heat-pumping performance. Here, we introduce a new design of an elastocaloric regenerator based on compression-loaded Ni–Ti tubes, referred to as a shell-and-tube-like elastocaloric regenerator. Our regenerator design, which can operate in both cooling and heat-pumping modes, enables durable operation and record performance with a maximum temperature span of 31.3 K in heat-pumping mode or maximum heating/cooling powers of more than 60 W, equivalent to 4,400 W/kg of the elastocaloric material (at temperature span of 10 K). In terms of both maximum performance metrics, these results surpass all previously developed caloric (magnetocaloric, electrocaloric, and elastocaloric) devices and demonstrate the enormous potential of compression-loaded elastocaloric regenerators to be used in elastocaloric devices for a wide range of cooling and heat-pumping applications.

## INTRODUCTION

Refrigeration (cooling, air conditioning, and heat pumping) is crucial for modern society; however, it is one of the most polluting sectors in the world. Cooling and air conditioning are nowadays responsible for 20% of the world's electricity consumption and 7.8% of all the greenhouse gas emissions,<sup>1</sup> but due to the rapid progress of developing countries combined with global warming trends, the refrigeration demands are increasing exponentially.<sup>2</sup> Besides cooling and air-conditioning, heat pumps for domestic and industrial heating are becoming an increasingly important renewable heating technology in an effort to eliminate coal/gas/petrol heating systems. However, refrigeration is almost exclusively based on vapor-compression technology, which is more than a century old and is one of the oldest electrically driven technologies still in use without a viable alternative.<sup>3,4</sup> Despite decades of development and continuous improvements, the efficiency of most (i.e., small-scale) vapor-compression systems remains relatively low,<sup>5,6</sup> and they still rely on environmentally harmful refrigerants.<sup>7</sup> Most refrigeration devices currently in use still utilize high global warming potential hydrofluorocarbons (HFCs), which must be phased out by the year 2047 according to the Kigali Amendment to the Montreal Protocol<sup>8</sup> and replaced by natural refrigerants only.

In the last two decades, a great scientific effort has been made to develop caloric cooling technologies based on the magnetocaloric, electrocaloric, elastocaloric,

## CONTEXT & SCALE

Refrigeration is vital to the modern society; however, it is one of the most polluting sectors in the world. Despite decades of development, our standard vapor-compression technology remains relatively inefficient and still uses harmful refrigerants. Elastocaloric cooling has shown significant potential as an environmentally benign alternative to the vapor-compression technology, but one of the biggest challenges to be solved is its limited fatigue life. Our new design of an elastocaloric regenerator made of compression-loaded Ni–Ti tubes enables buckling- and fatigue-resistant operation and record performance with commercially relevant cooling and heat-pumping characteristics. In terms of maximum specific cooling/heating performance metrics, it surpasses all previously developed caloric devices and demonstrates the enormous potential of compression-loaded elastocaloric devices for a wide range of cooling and heat-pumping applications.

and, more recently, barocaloric effect.<sup>9–13</sup> These technologies are based on solid-state phase transitions of ferroic materials that occur under the influence of external stimuli (e.g., magnetic field, electric field, and mechanical stress). They are potentially more efficient than vapor-compression technology<sup>14</sup> and considerably friendlier to the environment since they utilize environmentally benign solid-state refrigerants. The most advanced caloric technology today is magnetocaloric (magnetic) cooling. To date, about 100 magnetocaloric demonstrators and prototypes have been developed in universities and laboratories worldwide.<sup>14,15</sup> Despite some recent advances with demonstration of a magnetocaloric prototype achieving exergy efficiencies of more than 40% (at the temperature span of 7 K and the specific cooling power of around 115 W/kg of the magnetocaloric material),<sup>16</sup> magnetic cooling has not yet made the breakthrough necessary to meet the urgent global need for more efficient cooling. This is mainly due to the unavoidable use of expensive rare earth materials and the relatively low available latent heat of the magnetocaloric effect. Elastocaloric cooling, on the other hand, has shown very promising potential in recent years. It does not require expensive or toxic elements for operation and can produce very high temperature and entropy changes when elastocaloric materials (eCMs) are subjected to an external mechanical stress. Accordingly, elastocaloric cooling has been selected by the U.S. Department of Energy<sup>4</sup> and later also by the EU Commission<sup>17</sup> as the most promising future non-vapor-compression refrigeration technology.

Elastocaloric cooling is based on the elastocaloric effect (eCE), which is closely related to the superelasticity of shape-memory materials. In the case of shape-memory alloys, which are the most-studied eCMs, the eCE occurs due to a stress-induced martensitic transformation. When eCM is mechanically stressed (with external force), the transformation from an austenitic to a martensitic phase occurs. This is an exothermic transformation, resulting in the release of the latent heat and thus heating of the eCM under the adiabatic conditions. During unloading, the reverse martensitic-austenitic endothermic transformation occurs, leading to the absorption of the latent heat, which in the case of the adiabatic conditions, results in cooling of the material below the initial temperature.

The most-studied eCMs are binary Ni–Ti alloys, with which reproducible adiabatic temperature changes of about 25 K or even more could be achieved.<sup>18–21</sup> Alloying binary Ni–Ti with Cu, Fe, V, and/or Co has been shown to improve fatigue behavior and/or reduce hysteresis losses but at the expense of a smaller eCE.<sup>22–25</sup> The eCE has also been characterized in Cu-based<sup>26,27</sup> and Fe-based,<sup>28</sup> magnetic shape memory alloys<sup>29,30</sup> and shape memory polymers.<sup>31,32</sup> Recently, a new elastocaloric alloy (Ni–Mn–Ti–B) with a measured reversible adiabatic temperature change of 31.5 K was discovered, which is one of the largest directly measured caloric effects.<sup>33</sup> Recent reviews of eCMs can be found in the literature.<sup>34–38</sup>

To date, about 10 proof-of-the-concept elastocaloric devices have been developed and tested.<sup>15,34</sup> In general, they can be classified according to the heat transfer mechanisms, the applied thermodynamic cycles, and the loading modes.<sup>34</sup> Thus, we can distinguish between devices with a contact heat transfer between the eCM and the heat sink/source<sup>39–43</sup> and devices with a convective heat transfer between the eCM and the heat sink/source using a heat transfer medium.<sup>44–53</sup> We can also distinguish between single-stage devices,<sup>39,42,43,48</sup> where the temperature span between the heat sink and the heat source is limited by the adiabatic temperature change of the eCM and multi-stage devices, such as cascade,<sup>41,49</sup> heat recovery,<sup>44,45</sup> and active regeneration-based devices,<sup>46,47,50,52</sup> where the temperature span can

<sup>1</sup>Faculty of Mechanical Engineering, University of Ljubljana, Aškerčeva 6, 1000 Ljubljana, Slovenia

<sup>2</sup>Lead contact

\*Correspondence: [jaka.tusek@fs.uni-lj.si](mailto:jaka.tusek@fs.uni-lj.si)  
<https://doi.org/10.1016/j.joule.2022.08.011>

be increased beyond the adiabatic temperature change of the eCM. The latter is crucial for most practical applications where temperature span of more than 30 K is usually required. Most elastocaloric devices are based on tensile and compressive loading.<sup>34</sup> In terms of performance, the largest temperature span of any elastocaloric device to date was 28 K and was measured on a cascaded (3-stage) device using Ni–Ti wire under tension and convective heat transfer.<sup>49</sup> On the other hand, impressive specific cooling/heating powers of 19 W/g<sup>40</sup> and 20.9 W/g<sup>42</sup> of eCM were measured on single-stage, tension-loaded devices with contact heat transfer using Ni–Ti-based foil and natural rubber, respectively. Because these are single stage and rather miniature devices, their temperature span is limited by the adiabatic temperature change of the eCM and since they use a very small mass of eCM, their absolute cooling/heating power is less than 1 W. So far, the best elastocaloric performance has been thus obtained with the devices operating under tensile loading since they can use thin elastocaloric elements (wires, sheets, and foils) that allow for fast and efficient heat transfer between the eCM and the heat sink/source. On the other hand, eCMs are susceptible to fatigue under tension, resulting in a short lifetime of tension-based elastocaloric devices. It has been estimated<sup>18</sup> that an elastocaloric device should undergo several million loading cycles in a 10-year lifetime, whereas tensile-based devices typically fail after 10,000 cycles or even earlier.<sup>47,49,50</sup> It is well known that compressive loading can improve fatigue performance compared with tensile loading.<sup>54</sup> Several recent studies have shown that in compression, the eCM can reach well over 1 million cycles without any functional or structural fatigue.<sup>21,55–57</sup> However, developing an efficient and high performance compression-loaded elastocaloric device is challenging because thin-walled elastocaloric elements required for efficient heat transfer tend to buckle in compression, whereas thicker, more robust elements that would be mechanically stable cannot provide fast and efficient heat transfer and thus high performance when used in elastocaloric devices. To date, five elastocaloric devices loaded in compression have been developed. Three of them<sup>45,52,53</sup> are based on relatively long Ni–Ti tubes inserted into a housing that prevents the tubes from buckling, with the heat transfer fluid flowing inside the tubes, resulting in relatively poor heat transfer. The other two<sup>50,51</sup> are based on short mechanically stable tubes, with the heat transfer fluid flowing in a cross-flow around the tubes. Since the tubes are short, this results in a relatively low mass of the eCM and a small heat transfer area or, on the other hand, a high force required to induce the eCE if the number of the tubes is increased. Nevertheless, all compression-loaded elastocaloric devices have withstood several hundred thousand loading cycles (one of them<sup>51</sup> even  $10^7$  cycles) without significant functional degradation or fatigue failure but their overall performance (temperature span and specific cooling/heating power) is evidently lower compared with the best tensile-based elastocaloric devices. The largest measured temperature span for compression-loaded elastocaloric devices is 21.3 K (but the maximum specific cooling power is limited to 155 W/kg of the eCM),<sup>52</sup> whereas the maximum specific cooling power is 6,270 W/kg of the eCM (but with a limited maximum temperature span of 5.6 K).<sup>51</sup> A direct comparison of different caloric devices in terms of maximum temperature span and maximum specific cooling/heating power is presented in the [results and discussion](#) section.

In this paper, we present for the first time an elastocaloric regenerative device that is fatigue-resistant, yet powerful and efficient, with a maximum specific performance metrics that particularly in the heat-pumping mode surpasses all previously developed caloric cooling and heat-pumping devices. We introduce a new design of an active elastocaloric regenerator made of Ni–Ti tubes that allows for functionally stable cyclic compressive loading and fatigue-resistant operation (due to compression)

and also good heat transfer characteristics. Such a design is reminiscent of the well-known shell-and-tube heat exchanger and is thus referred to as shell-and-tube-like elastocaloric regenerator. It provided a record performance with a maximum temperature span of 31.3 K in heat-pumping mode (at zero cooling/heating power) or maximum heating/cooling powers of more than 60 W, equivalent to 4,400 W/kg (at temperature spans of up to 10 K), using only 13.7 g of the eCM. The regenerator has demonstrated fatigue-resistant operation with more than 300,000 loading cycles at the stress levels of up to 825 MPa, with no signs of performance degradation when operating in cooling or heat-pumping mode over a wide temperature range.

## RESULTS AND DISCUSSION

### Design and operation of a shell-and-tube-like elastocaloric regenerator

The operation of the shell-and-tube-like elastocaloric regenerator developed in this work follows the active elastocaloric regeneration principle originally presented in Tušek et al.<sup>58</sup> and experimentally demonstrated for a tensile-loaded regenerator.<sup>46</sup> The concept of the active caloric regeneration was first applied in magnetic refrigeration and remains the most promising concept for exploiting the magnetocaloric effect in magnetic refrigerators.<sup>14</sup> In the recent years, the concept of the active caloric regeneration was successfully applied also in electrocaloric<sup>59</sup> and elastocaloric technologies.<sup>46</sup> The active elastocaloric regenerator is a porous structure made of eCM through which a heat transfer fluid (e.g., water) is pumped in a counter-flow direction between a heat sink and a heat source. The elastocaloric regenerator has a dual function in an elastocaloric device; it acts as a refrigerant, since it contains an active eCM, and as a regenerator allowing an increase of the temperature span between heat sink and heat source, which can be several times larger than the adiabatic temperature change of the eCM itself. [Figures 1A–1D](#) show the four basic operating steps of a compression-loaded shell-and-tube-like elastocaloric regenerator in the case of the Brayton thermodynamic cycle, which is the most widely used thermodynamic cycle in caloric cooling.<sup>14</sup> In addition to the elastocaloric regenerator, the setup includes a piston pump that generates a fluid flow through the regenerator, a series of check valves (V) that control the direction of the fluid flow, and two external heat exchangers, namely a cold external heat exchanger (CHEX) and a hot external heat exchanger (HHEX), through which heat is absorbed and transferred from/to the environment. In the first step ([Figure 1A](#)), the regenerator is adiabatically loaded (strained) by the external force, causing the eCE and thus the heating of the eCM in the regenerator. In the second step ([Figure 1B](#)), the piston pumps the fluid from the CHEX through the loaded regenerator toward the HHEX (check valves V1 and V3 are open). Due to the heat transfer in the regenerator, the fluid heats up and releases the heat to the environment in the HHEX. In the third step ([Figure 1C](#)), the regenerator is adiabatically unloaded (the external force is removed), causing the eCM in the regenerator to cool down due to the eCE. In the fourth step ([Figure 1D](#)), the piston pumps the fluid in the counterflow direction from the HHEX through the unloaded regenerator toward the CHEX (check valves V2 and V4 are open), where the cold fluid, cooled in the regenerator, absorbs the heat from the environment. When these four steps are continuously repeated, a temperature profile is established along the regenerator.

[Figure 2](#) shows the CAD model and the photo of the actual shell-and-tube-like elastocaloric regenerator. The basic idea of this design is to use a series of elastocaloric tubes inserted into supporting elements (baffles), similar to the well-known shell-and-tube heat exchanger. In such a configuration of an active elastocaloric regenerator, the baffles act as supporting elements that prevent the tubes from buckling

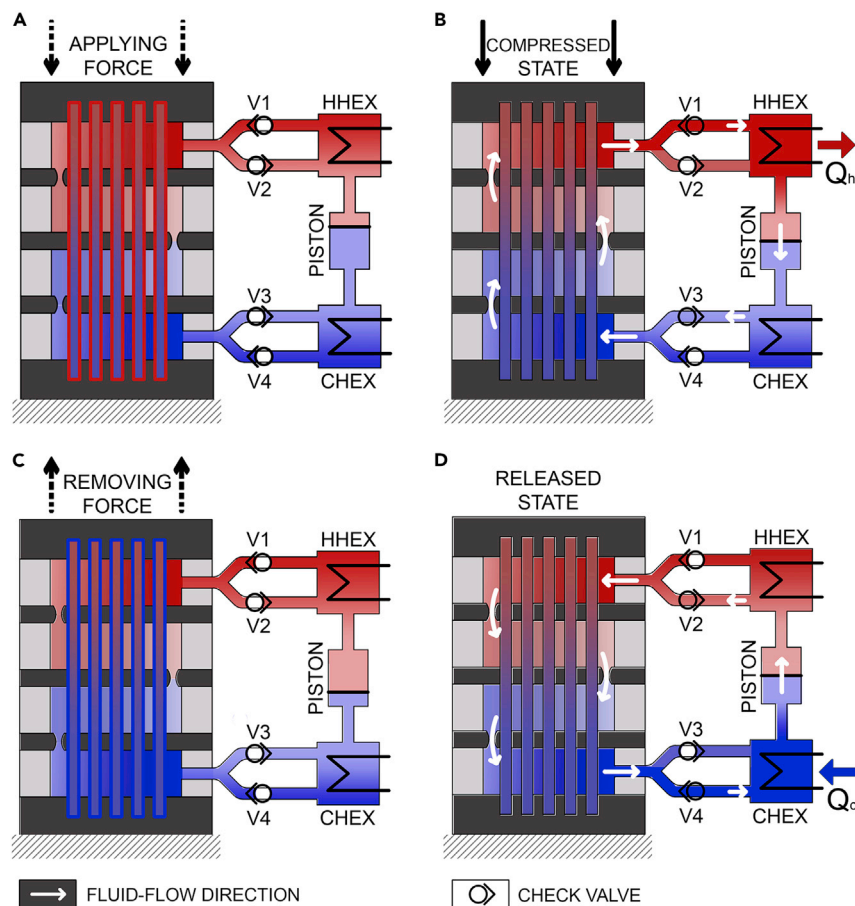


**Figure 1. Schematic presentation of four basic operational steps of the shell-and-tube-like elastocaloric regenerator**

- (A) Mechanical loading of the regenerator by applying the external force.  
 (B) Fluid flow from the CHEX toward the HHEX where the heat is released to the hot environment.  
 (C) Unloading of the regenerator by removing the external force.  
 (D) Fluid flow from the HHEX toward the CHEX where the heat is absorbed from the cold environment.

and, at the same time, guide the heat transfer fluid in cross-flow over the tube bundles (on the shell side), as schematically shown in Figure 1. Prior to applying this geometry as an active elastocaloric regenerator, we have characterized its thermo-hydraulic properties under oscillating-flow conditions.<sup>60</sup> Details of the regenerator design can be found in the [experimental procedures](#) section.

The regenerator was tested in a new in-house developed experimental setup, which is presented in the [supplemental information \(Note S1; Figures S1 and S2\)](#), where the associated measurement uncertainties are shown as well ([Note S2; Table S1](#)). It should be noted that the main goal of this experimental setup was to provide suitable and variable operating conditions to the regenerator in a range of high forces and small strokes. Since the efficiency of the experimental setup itself was not crucial at this stage, we have applied a hydraulic actuator, which is the most suitable/flexible driving mechanism for assuring required operating conditions. Figure 3 shows an example of the IR images captured during the operation of the regenerator in the heat-pumping mode under the selected operating conditions. The inlet temperature on the cold side was around 20°C, whereas the temperature on the hot side

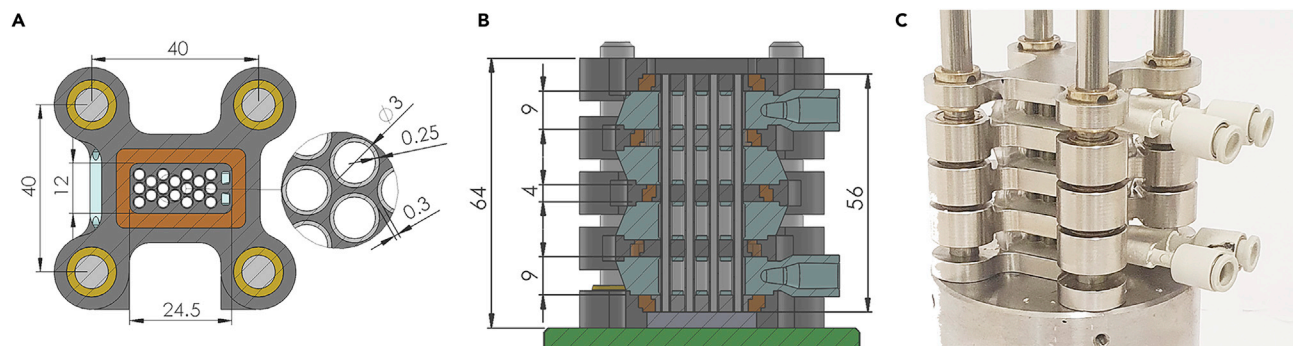


**Figure 2. Design of the shell-and-tube-like elastocaloric regenerator**

(A and B) CAD model of the regenerator showing (A) cross-sectional and (F) longitudinal view. (C) Photo of the actual regenerator.

was increasing during the operation and reached about 43°C in the steady-state conditions. In further experiments, to demonstrate full capability of the regenerator, it was tested in both heat-pumping and cooling modes, which is important for several potential applications (e.g., electric vehicles) where the same system needs to provide both cooling and heating. It should be noted that the cold-side temperature in the heat-pumping mode (heat source) and the hot-side temperature in the cooling mode (heat sink) were different in order to better approach real temperature levels of cooling and heat-pumping applications and were maintained at 20°C and 30°C, respectively. The ambient temperature was maintained at 25°C ± 1.5°C for all the tests, by which we assure similar heat losses/gains for both operating modes. However, in both operating modes, the regenerator was tested under different operating conditions, namely different stress levels ( $\sigma$ ), different operating frequencies ( $f$ ), different displaced fluid volume ratios ( $V^*$ ), and different cooling/heating powers, using distilled water as a heat transfer fluid—see [experimental procedures](#) section for more details. The displaced fluid volume ratio ( $V^*$ ) is defined as the ratio between the fluid volume in the regenerator and the fluid volume displaced through the regenerator in a single fluid flow period (see Equation 1). In all experiments, the maximum applied stress was limited to 825 MPa, which corresponds to an applied force of 32 kN. Our preliminary results on this regenerator geometry (i.e., a test regenerator) revealed that the tubes show the beginning of structural instabilities at stresses above 850 MPa (based on naked eye observations) and collapsed at stress of 950 MPa due to buckling. The results of mechanical behavior and buckling analysis of the test regenerator are shown in the [supplemental information](#) (Note S3; Figures S3 and S4). Although we have shown<sup>21</sup> that a single tube of the same material and dimensions is mechanically stable up to stresses of 1,200 MPa, the complex mechanical behavior in the shell-and-tube-like elastocaloric regenerator (longer tubes supported by baffles and related geometric inaccuracies and tolerances) reduces the mechanical stability and critical buckling stresses to some extent, compared with a single tube.

Before testing the regenerator for cooling and heat-pumping performance, we also measured the eCE of the eCM in the regenerator. These preliminary tests were conducted only up to the limited stress level of 800 MPa in order not to overstress the regenerator and not to induce pronounced buckling instabilities (as demonstrated by the test regenerator in Figure S4 in the [supplemental information](#)) before being tested for cooling and heat-pumping performance. The results of the preliminary tests are shown in the [supplemental information](#) (Note S4; Figures S5 and S6) in

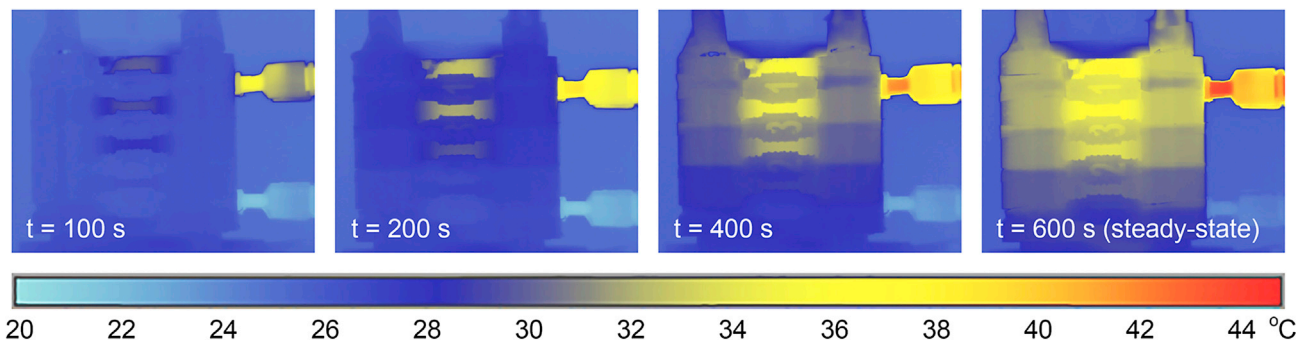


**Figure 3.** IR images (captured with the FLIR A6750sc IR camera) of the elastocaloric regenerator in the heat-pumping mode from the initial state until the steady-state is reached (for the IR video of the operation, see [Video S1](#))

the form of stress-strain diagrams, adiabatic temperature changes, and material coefficient of performance (COP) values. Moreover, [Figure S5](#) also includes the eCE and the material's COP values of a single Ni–Ti tube of the same batch.<sup>21</sup> One can see from [Figure S5](#) that the elastocaloric properties of the single tube and the regenerator are somewhat different but still comparable. This can be attributed to a small degree of buckling of the tubes in the regenerator, which was not observed by the naked eye under these conditions but can be detected in the IR images of the tubes in the regenerator captured during loading and unloading ([Figure S6](#)). This results in a somewhat smaller transformation of the tubes and thus smaller adiabatic temperature changes and smaller hysteresis loop area of the regenerator compared with the single tube with a smaller (or zero) degree of buckling (see [Note S4](#) for details).

### Maximum temperature span

In the first series of tests, the objective was to determine the maximum temperature span without adding any thermal loads to the system (i.e., without cooling or heating power). The tests were conducted under various operating conditions in both cooling and heat-pumping modes, as shown in [Figure 4](#). [Figures 4A](#) and [4B](#) show examples of the time evolution of the temperature span from an initial to a steady-state at selected operating conditions in heat-pumping and cooling modes, respectively. Note that in the examples shown in [Figures 4A](#) and [4B](#), the displaced fluid volume ratio ( $V^*$ ) was larger in the cooling mode, which resulted in larger temperature fluctuations at the outlets of the regenerator compared with the heat-pumping mode. Remarkably, a temperature span of 31.3 K was achieved in the heat-pumping mode, which is the largest temperature span achieved by any elastocaloric device to date. [Figures 4C](#) and [4D](#) show the temperature spans as a function of the displaced fluid volume ratio measured at different operating frequencies (0.48, 0.9, and 2 Hz) and two different applied stress levels (775 and 825 MPa). It is evident that, compared with the cooling mode, larger temperature spans can be achieved in the heat-pumping mode. This can be clearly seen also in [Figure 3E](#), which shows the temperature spans as a function of the applied stress for both cooling and heat-pumping modes. Although somewhat better heat-pumping performance compared with cooling was expected<sup>14</sup> (input work is converted into heat), there are additional sources of irreversibility that cause these trends. The first is that the eCE itself in Ni–Ti is not fully reversible. Namely, due to the hysteresis losses, the positive adiabatic temperature changes during loading are larger than the negative adiabatic temperature changes during unloading.<sup>20,21</sup> In addition, since the empty volume of the regenerator is reduced during loading (the outer diameter of the tubes is increased and the spacing between them is thus decreased), this results in a smaller hydraulic

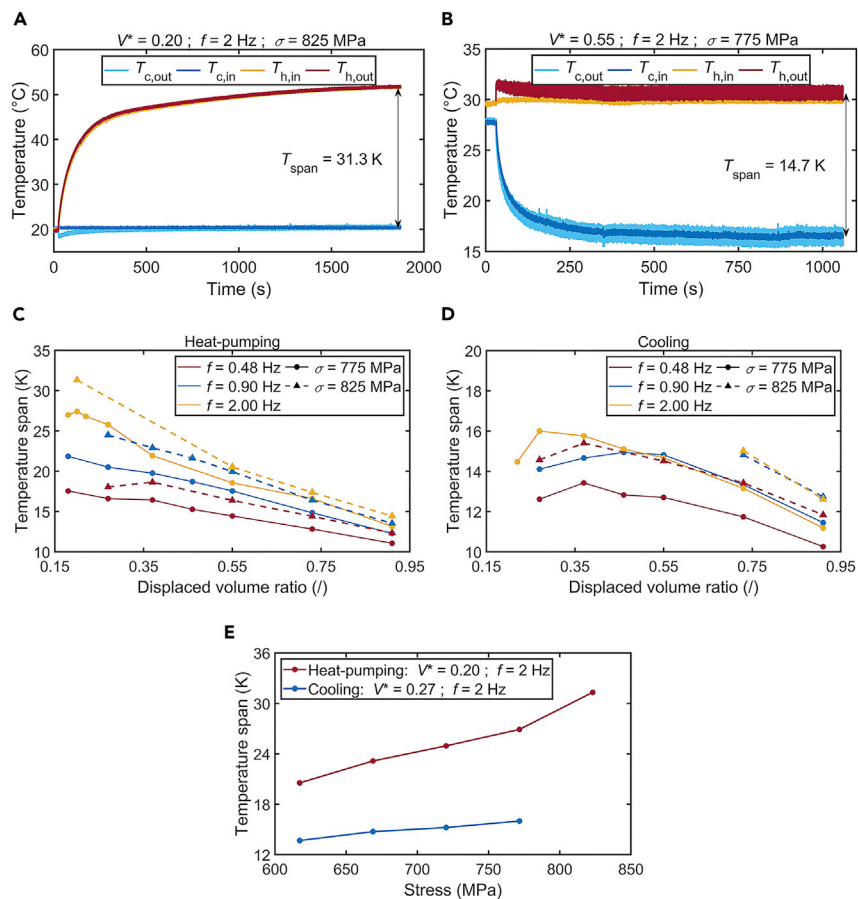


**Figure 4. Maximum temperature span of the elastocaloric regenerator without adding any cooling/heating power to the system**

(A and B) Time evolution of the temperature span in (A) the heat-pumping mode and (B) the cooling mode.

(C and D) Temperature span as a function of the displaced fluid volume ratio in (C) the heat-pumping mode and (D) the cooling mode.

(E) Temperature span as a function of the applied stress for the cooling and the heat-pumping modes.

diameter and more intense heat transfer during the fluid flow toward HEX and thus improves the heat-pumping performance compared with the cooling. The third potential reason is some internal friction in the regenerator, e.g., between the baffles and the tubes, which could additionally heat up the regenerator to some extent. As can be seen in Figure 4E, the difference between the temperature span in the heat-pumping and the cooling modes increases with increasing stress, which is due to the gradual increase of all three above-mentioned potential irreversibility sources with increasing stress. Since the direct impact of different irreversibility sources on the regenerator performance cannot be evaluated solely based on the obtained experimental data, a comprehensive numerical modeling<sup>14,60</sup> is currently in progress to better understand the different sources of irreversibilities and their impact on the regenerator performance. Moreover, it is important to note that the cold-side temperature was limited to about 15°C and the operating conditions that would lead to higher temperature spans were not applied in the cooling mode, as shown in Figures 4D and 4E. This is due to the relatively high austenite finish temperature (i.e., the temperature above which the reverse martensitic

transformation is completed) of the Ni–Ti tubes used in the regenerator (about  $-7^{\circ}\text{C}$ ). Since the negative adiabatic temperature change after the unloading can be as high as 20 K,<sup>21</sup> and we wanted to prevent the temperature of the eCM from dropping below the austenite finish temperature at any stage of the cycle, the temperature limit of about  $15^{\circ}\text{C}$  was applied at the cold side of the regenerator. Lower temperatures would cause the temperature of the eCM on the cold side to temporarily drop below the austenite finish temperature immediately after the unloading, resulting in a temporary residual strain of the tubes and consequently not fully reversed superelasticity.<sup>10</sup> This is highly undesirable, as it would lead to certain technical difficulties in the operation of the regenerator (e.g., non-uniform movement of the baffles and the tubes), which we wanted to avoid. However, the applied Ni–Ti tubes are not suitable for the temperatures below around  $15^{\circ}\text{C}$ . Larger temperature spans in cooling mode would be possible if Ni–Ti with a lower austenite finish temperature was used (see, e.g., Frenzel et al.<sup>61</sup>).

As can be seen in [Figures 4C](#) and [4D](#), higher stress levels allow for a larger temperature span for all frequencies and displaced fluid volume ratios because a larger applied stress results in a larger eCE and thus in larger adiabatic temperature changes. It can also be seen that the temperature spans increase with operating frequency for all displaced fluid volume ratios. The largest temperature spans were obtained at the highest applied frequency (2 Hz), which corresponds to a single fluid flow period of 0.2 s. According to the trends shown in [Figure 4C](#), even larger temperature spans can be expected in the heat-pumping mode if the operating frequency was increased further. Another important parameter that has a significant impact on the performance of an elastocaloric regenerator and its temperature span is the displaced fluid volume ratio. As can be seen in [Figures 4C](#) and [4D](#), the optimal displaced fluid volume ratio in the heat-pumping mode is about 0.2, whereas in the cooling mode, it is slightly larger (between 0.3 and 0.4). This means that in the heat-pumping mode only 20% of the fluid volume in the regenerator should be displaced in a single flow period to achieve the largest temperature span. However, the reason for the different optimal displaced fluid volume ratios in heat-pumping and cooling modes is related to the definition of the displaced fluid volume ratio itself. Note that it is defined based on the geometry of the regenerator in the unloaded condition (see [Equation 1](#)). The volume reduction that occurs during loading of the regenerator cannot be precisely defined and is therefore not considered in the definition of the displaced fluid volume ratio.

Based on the measured temperature spans regeneration factors (i.e., the ratio between the temperature span of the regenerator and the adiabatic temperature change of the eCM) were assessed. The regeneration factors were calculated on the basis of the adiabatic temperature changes measured on the single tube of the same batch<sup>21</sup>—see [Figure S5](#) in the [supplemental information](#). At the stress level of 825 MPa, the adiabatic temperature changes are about 18 K upon loading and 15 K upon unloading, which means that the regeneration factor is around 1.7 in the heat-pumping mode (calculated based on adiabatic temperature change during loading) and slightly above 1 in the cooling mode (calculated based on adiabatic temperature change during unloading). Note that in the cooling mode, we were not able to reach the optimal performance due to the limitations related to too high values of the austenite finish temperature. As shown in [Torello and Defay](#),<sup>62</sup> the regeneration factors of active magnetocaloric regenerators can be up to 10, whereas the parallel-plate active elastocaloric regenerator loaded in tension had the regeneration factor of around 1.8. However, although a high regeneration factor is required in the case of low adiabatic temperature changes, a high regeneration factor essentially

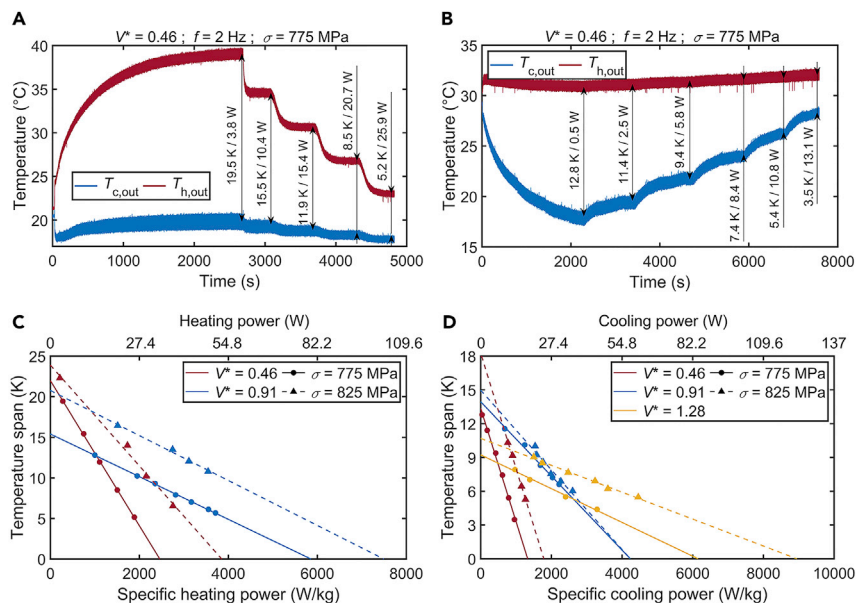


**Figure 5. Cooling and heating powers of the elastocaloric regenerator**

(A and B) Time evolution of the temperature span due to the gradual increase of (A) the heating power in the heat-pumping mode and (B) the cooling power in the cooling mode.

(C) Temperature span—(specific) heating power characteristics at different operating conditions.

(D) Temperature span—(specific) cooling power characteristics at different operating conditions.

means that a significant amount of a caloric material in the regenerator contributes only to the establishment of the temperature span and does not contribute to the generation of the useful cooling or heating power (resulting in a low specific cooling/heating power). Therefore, in the case of pronounced caloric effect (such as in the case of eCE this work), relatively low regeneration factor, which due to the relatively high adiabatic temperature changes allow for establishing large temperature spans, results in higher specific cooling/heating powers compared with the caloric regenerators with higher regeneration factors.

### Cooling/heating power and efficiency

In the second series of experiments, two additional heat exchangers were added to the experimental setup, through which a thermal load was supplied to the regenerator, simulating heating power in the heat-pumping mode and cooling power in the cooling mode, as described in the [supplemental information \(Note S1\)](#). [Figures 5A](#) and [5B](#) show an example of the time evolution of the temperature span between both fluid outlets of the regenerator when the heating power in the heat-pumping mode ([Figure 5A](#)) and the cooling power in the cooling mode ([Figure 5B](#)) were gradually supplied to the system. The procedure for calculating the cooling/heating power is explained in the [experimental procedures](#) section (Equation 4). As expected,<sup>14</sup> the temperature span decreases with increasing the cooling/heating power. [Figures 5C](#) and [5D](#) show linear dependence of the temperature span and the (specific) cooling/heating power, as normally observed for (single-layered) caloric devices.<sup>14</sup> The experiments were performed at the operating frequency of 2 Hz, considering two different stress levels and different displaced fluid volume ratios. A small displaced fluid volume ratio allows for larger maximum temperature spans, but a steeper slope of the temperature span—cooling/heating power characteristics at the same stress level. This results in lower maximum (specific) cooling/heating

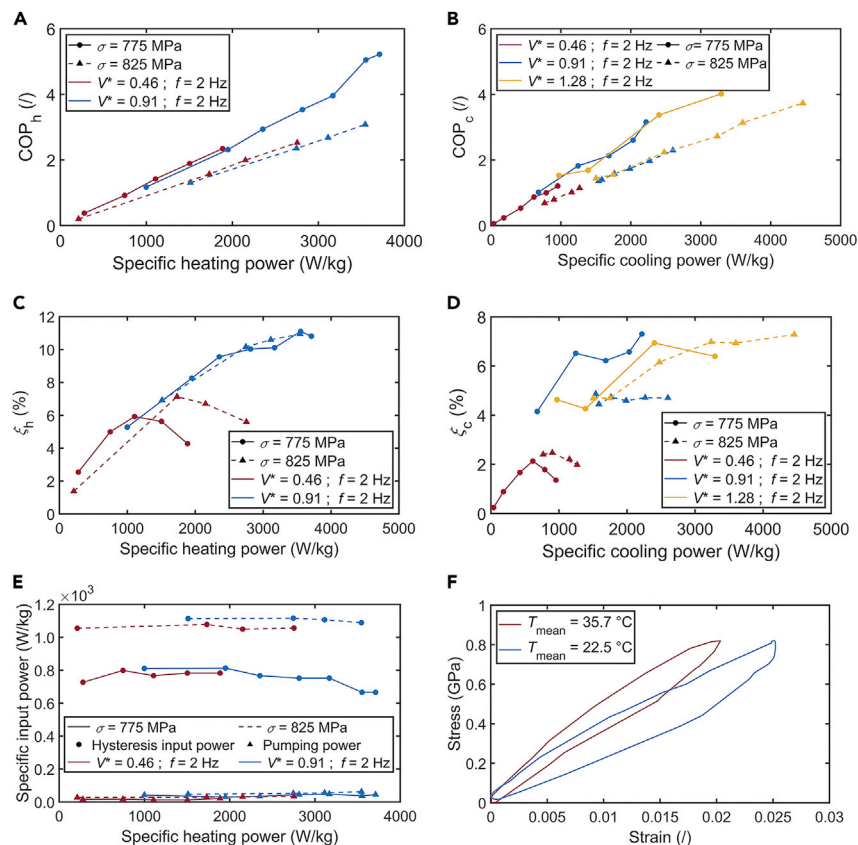


**Figure 6. The efficiency of the elastocaloric regenerator**

- (A) Heating COP values as a function of the specific heating power.  
 (B) Cooling COP values as a function of the specific cooling power.  
 (C) Heating exergy efficiency as a function of the specific heating power.  
 (D) Cooling exergy efficiency as a function of the specific cooling power.  
 (E) Specific input mechanical and pumping power as a function of the specific heating power (for the heat-pumping mode).  
 (F) An example of the stress-strain curves in the heat-pumping mode (at the regenerator's mean temperature of  $35.7^\circ\text{C}$ ) and in the cooling mode (at the regenerator's mean temperature of  $22.5^\circ\text{C}$ ).

powers compared with larger values of the displaced fluid volume ratio, which on the other hand allows for smaller maximum temperature spans. Thus, one can change the performance of the regenerator between a high temperature span performance and a high cooling/heating power performance by changing the amount of the heat transfer fluid pumped through the regenerator during the flow period (i.e., the displaced fluid volume ratio). Increasing the stress level from 775 to 825 MPa does not significantly affect the slope of the temperature span—cooling/heating power characteristics but the performance is—at the same operating frequency and displaced fluid volume ratio, shifted to larger temperature spans and larger cooling/heating powers. It should be noted that due to the system constraints, the largest applied cooling and heating powers were limited to about 60 W, corresponding to 4,400 W/kg of the eCM. However, according to the characteristics shown in Figures 5C and 5D, cooling/heating powers of more than 100 W could be achieved at zero temperature span (with a displaced fluid volume ratio of above 1 and a stress level of 825 MPa). Remarkably, in the heat-pumping mode, heating power of about 51 W (3,700 W/kg of the eCM) was measured at the temperature span of 12 K (see Figure 5C).

Based on the cooling/heating performance, the regenerator's efficiency was further evaluated (see [Figure 6](#)). The efficiency of a cooling/heat-pumping system is usually expressed by the COP and the exergy efficiency, the calculation procedures of which are described in the [experimental procedures](#) section (Equations 5, 6, 7, and 8). The power supplied to the system includes the power required to pump the fluid, which is calculated based on the pressure drop measurements across the system during the fluid flow periods, and the applied mechanical power (see Equations 6 and 7). It has to be emphasized that a complete recovery of the mechanical work is assumed here, which is a common assumption in the efficiency analysis of the elastocaloric devices.<sup>34,40,44,46,48,49,53</sup> Namely, it is assumed that the work released during the unloading is fully recovered. The input mechanical work is thus related only to its unrecoverable part, which is essentially an enclosed area of the stress-strain diagram (the hysteresis loop area). The work recovery can be achieved by applying multiple phase-shifted elastocaloric regenerators as antagonistic pairs (see Bruederlin et al.<sup>40</sup> and Qian et al.<sup>44</sup>) or in a rotating elastocaloric device.<sup>48</sup> In such configurations, the work released during the unloading of one (or more) elastocaloric regenerator(s) can be directly used to provide (a significant portion of) the loading work for the other regenerator(s) and vice versa.<sup>34</sup>

[Figures 6A–6C](#) show the COP values and the exergy efficiencies as a function of the cooling/heating power under different operating conditions. As expected from basic thermodynamics,<sup>14</sup> the elastocaloric regenerator operates more efficiently, i.e., with higher COP values and better exergy efficiencies, when operating in the heat-pumping mode, where COP values of up to 5.2 and exergy efficiencies of up to 11% were obtained at a specific heating power of around 3,700 W/kg (see [Figures 6A](#) and [6C](#)) and a temperature span of about 5 K (see [Figure 5C](#)). At lower temperature spans, even higher COP values could be expected if higher heating/cooling powers were applied. As shown in [Figure S5](#) in the [supplemental information](#), the material COP values of the Ni–Ti tubes used in the regenerator range from 5 to 6 (at similar stresses), which represents the upper COP limit of this material when operating in the cooling/heat-pumping device. As expected, some additional losses occurred in the elastocaloric regenerator, e.g., heat transfer losses, losses due to the temperature span generation, friction losses, etc., but it seems that these are not critical and still allow for a relatively efficient operation. To achieve higher device's COP values, it is therefore crucial to use a more efficient eCM with lower hysteresis losses but preferably not at the expenses of the high eCE as usually observed.<sup>63</sup> As can be seen in [Figures 6A](#) and [6B](#), the displaced fluid volume ratio does not affect the COP-specific cooling/heating power characteristics, which remain linear and practically unchanged for all values of the displaced fluid volume ratios. It has to be emphasized that as the cooling/heating power increases, the temperature span decreases (see [Figures 5C](#) and [5D](#)), and therefore, high COP values are related to low temperature spans. However, the independence of the COP-specific cooling/heating power characteristics of the displaced fluid volume ratio is closely related to the behavior of the mechanical input power (see [Figure 6E](#)), which remains similar for all evaluated displaced fluid volume ratios and the applied heating/cooling powers. [Figure 6E](#) also shows the power required to pump the fluid through the system. It increases as the displaced fluid volume ratio increases but its contribution to the total input power is minor and its effect on the COP values is therefore small.

[Figure 6F](#) shows an example of the stress-strain responses of the elastocaloric regenerator operating in the heat-pumping mode (with  $T_{\text{mean}}$  of 35.7°C) and in the cooling mode (with  $T_{\text{mean}}$  of 22.5°C). Since the superelastic and thus the elastocaloric response of shape-memory alloys are strongly temperature dependent, the

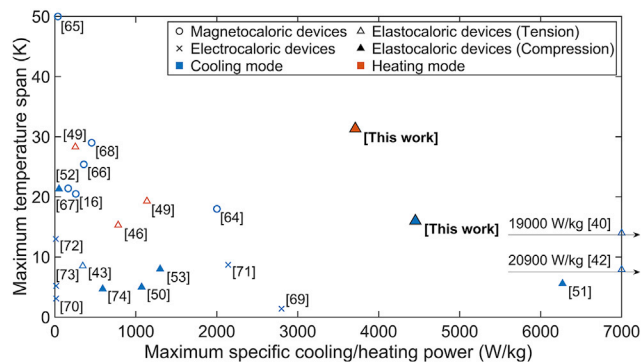


**Figure 7. A comparison of the maximum temperature span and the maximum specific cooling/heating power of the best magnetocaloric (magnetic),<sup>16,64–68</sup> elastocaloric,<sup>40,42,43,46,49–53,74</sup> and electrocaloric<sup>69–73</sup> cooling and heat-pumping devices developed to date**

stress-strain response is affected by the temperature of the eCM in the regenerator. As shown in Figure 6F, for the same stress level, the elastocaloric regenerator exhibits different stress-strain behaviors, namely lower strain, when operated at a higher temperature (in heat-pumping mode) compared with a lower temperature (in cooling mode). This behavior affects the mechanical input power, and thus, the COP values to some extent. However, since most of the tests were performed at average temperatures of the eCM between 20°C and 30°C, this influence is rather minor in our case.

It is also interesting to note that for the same cooling/heating power (but at different temperature spans), a lower applied stress enables higher COP values. Similar trends have been observed at the material level (see Figure S5 in the supplemental information), where the COP values of an eCM decrease with the applied strain/stress, since the input work increases by a larger amount than the cooling/heating energy, when the applied stress is increased.

The exergy or the second law efficiency (see Figures 6C and 6D) is an important measure of the system's efficiency because it gives the ratio between the actual COP and the maximum COP (i.e., the Carnot COP) that would theoretically be possible at a given temperature span. Figures 6C and 6D show that the exergy efficiency generally increases with increasing the displaced fluid volume ratio and is not significantly affected by the applied stress level. The maximum exergy efficiencies of about 11% and 7% were achieved in the heat-pumping and the cooling modes, respectively.

Finally, although a small degree of buckling was observed in the preliminary tests of the shell-and-tube-like elastocaloric regenerator, it withstood more than 300,000 cycles at stress levels up to 825 MPa, when operated over a wide temperature range (between 14°C and 51°C), in both, cooling and heat-pumping modes, without structural or functional fatigue. An example of the mechanical behavior of the regenerator during cycling under different operating conditions is shown in the supplemental information (Note S5; Figure S7), from which one can see that no degradation of mechanical behavior occurred. The critical stress that led to the buckling failure of the tubes in this regenerator was found to be approximately 940 MPa.

### Performance comparison with the state-of-the-art caloric devices

Comparing the performance of our shell-and-tube-like elastocaloric regenerator with other caloric devices developed to date reveals its excellent performance. Figure 7 shows a comparison of the two most important performance metrics, namely the

maximum temperature span and the maximum specific cooling/heating power (per unit mass of the caloric material used) of the best caloric (magnetocaloric, electrocaloric, and elastocaloric) cooling and heat-pumping devices developed and tested so far. Note that due to some inevitable irreversibilities in caloric devices, the heat-pumping performance is expected to be somewhat better than the cooling performance (as also demonstrated in this work). The COP values were not used for the comparison since the methodology used for the calculation of COP (particularly the input work) is not standardized, and therefore, a direct comparison of different devices from the COP point of view would not be representative. It should be noted that [Figure 7](#) shows the maximum temperature span and maximum specific cooling/heating power achieved by different caloric devices, values of which were not achieved simultaneously, but they present the maximum capabilities of the system and the operational extremes in between which the performance can be changed by changing the operating conditions. As mentioned above, the maximum temperature span is achieved at zero cooling/heating power, whereas the maximum specific cooling power is achieved at zero temperature span. However, most of the caloric devices presented in [Figure 7](#) (except,<sup>64</sup> which uses multilayer active magnetic regenerators) have a linear or nearly linear temperature span—cooling/heating power characteristics (see [Figure 5](#) for example). Assuming a linear relation between the maximum temperature span and the maximum specific cooling/heating power, an approximate full performance characteristic can be derived for each caloric device in [Figure 7](#).

Nevertheless, in terms of both operation extremes, namely the maximum temperature span and the maximum specific cooling/heating power, the shell-and-tube-like elastocaloric regenerator developed in this work outperforms (particularly in the heat-pumping mode) all other caloric cooling and heat-pumping devices, as shown in [Figure 7](#). One magnetocaloric device<sup>65</sup> generated a larger maximum temperature span but a very small maximum specific cooling power. On the other hand, two elastocaloric devices<sup>40,42</sup> have produced very high specific cooling powers of around 20,000 W/kg of the eCM, but since they are both miniature single-stage devices, they have limited temperature spans and absolute cooling powers below 1 W. However, it should be noted that the best magnetocaloric devices can achieve cooling/heating powers close to or even above 1 kW,<sup>16,64,66,67</sup> but they use more than 1 kg of the magnetocaloric material, resulting in small specific cooling/heating powers (see [Figure 7](#)), which limits their commercial potential.

### Outlook

Despite very promising results, further improvements of the shell-and-tube-like elastocaloric regenerator are possible, both at the material level and in the regenerator design. Regarding the material, in addition to the application of eCMs with well-suited austenite finish temperatures for the target temperature ranges, eCMs with lower hysteresis losses are highly desirable, which is crucial for more efficient future elastocaloric devices. From the regenerator design point of view, the improvements should be in the direction of reducing the thermal mass of the housing and the supporting elements (baffles), in order to reduce the longitudinal thermal conductivity and the parasitic losses to the environment, but without compromising the stability of the tubes and the whole structure of the regenerator. Although the dimensions of the tubes used in the regenerator represent a relatively good compromise between the buckling stability and the heat transfer capabilities, further improvements by using mechanically stable tubes with smaller wall thicknesses are possible, which can be achieved through a better combination of slenderness and the thickness-to-diameter ratio of the tubes. However, a fundamental limitation of the shell-and-tube-like elastocaloric regenerator presented in this work is the reduced heat transfer area, since the heat transfer fluid only

flows around the tubes, whereas the inside surface of the tubes is not in contact with a heat transfer fluid and is therefore not directly used for the heat transfer. Alternative and more advanced geometries of the same concept would therefore further improve the performance of the regenerator. On the other hand, an important advantage of the shell-and-tube-like regenerator design is its scalability. Namely, the length of the regenerator could be increased without increasing its cross-sectional area. This would increase the mass of the eCM, and thus, its absolute cooling/heating power and temperature span but due to the same cross-sectional area, the operating forces would remain unchanged. This is very important, since excessive required forces could become a bottleneck for the elastocaloric technology.

Finally, the proposed and possibly further improved shell-and-tube-like elastocaloric regenerator(s) will be used in a rotating elastocaloric device driven by a suitable and highly efficient drive system.<sup>75,76</sup> The rotating device will also use the principle of work recovery to directly utilize the work released during the unloading, which is crucial for highly efficient elastocaloric devices and would also allow smaller required torque and more compact design.

## EXPERIMENTAL PROCEDURES

### Resource availability

#### Lead contact

Further information and requests for resources and materials should be directed to and will be fulfilled by the lead contact, Jaka Tušek ([jaka.tusek@fs.uni-lj.si](mailto:jaka.tusek@fs.uni-lj.si)).

#### Materials availability

This study did not generate new unique materials.

#### Data and code availability

The datasets presented in this study are available from the lead contact upon reasonable request.

### Regenerator design details

The design of the regenerator is shown in [Figure 2](#). It consists of 18 Ni–Ti tubes with 55.92 wt % Ni, an austenite finish temperature ( $A_f$ ) of  $-7.3^\circ\text{C}$  (determined by bend and free recovery method in accordance with ASTM F2082 standard), an outer diameter of  $3.0 \pm 0.01$  mm and an inner diameter of  $2.5 \pm 0.025$  mm, supplied by Memry Corporation (SAES Group). The outer surfaces of the tubes were centerless ground and the inner surfaces are oxide free. The total mass of the tubes was 13.7 g. Further details on the material properties of the tubes, eCE, buckling stability, and fatigue performance can be found in Porenta et al.<sup>21</sup> The tubes were cut to a length of  $56 \pm 0.01$  mm using Buehler IsoMet low-speed diamond saw with low cutting force to avoid overheating of the material, which can lead to microstructural changes and loss of superelasticity. The cut surfaces of the tubes were then polished using Buehler EcoMet30 and P800 grit sandpapers. The tubes were inserted with precise fit with small clearance into five 4 mm-thick baffles evenly distributed along the length of the tubes (see [Figure 2](#)). The gauge length (i.e., the free length between the baffles) of the tubes was 9 mm, which, according to our preliminary buckling analysis on a single tube of the same geometry, resulted in functionally stable behavior with no signs of buckling under compression over the entire transformation plateau (up to 1,200 MPa).<sup>21</sup> A staggered arrangement of the tubes was chosen because this configuration allows for higher packing density with better heat transfer properties compared with a linear arrangement.<sup>77</sup> The baffles were fabricated using a precision milling process. They were made of austenitic stainless steel (1.4307, X2CrNi18-9) and laminated with a

polyetheretherketone (PEEK) layer to reduce heat losses through the guiding rods to the environment (see [Figure 2A](#)). Each baffle was guided by a set of bronze bushings (Meusburger E5156/8/12/10) on the four guiding rods to provide uniaxial loading and prevent global buckling of the regenerator. The housing, located around the tube bundle and between each baffle (see [Figure 2](#)), was additively manufactured with a Formlabs Form 2 using Formlabs Elastic 50A material with high elasticity to follow the deformation of the regenerator. The inner wall of the housing has a contour corresponding to the circumference of the tube bundle. The spacing between the inner wall of the housing and the tube bundle was similar to the spacing between the tubes (i.e., 0.3 mm). Finally, the regenerator was thermally insulated with insulating foam (except for the test where the IR camera was used—see [Figure 3](#)), whereas a 10 mm thick layer of PEEK was used at both ends of the regenerator to reduce the thermal conduction and heat losses through the metallic loading and stationary heads.

### Testing procedure/operating conditions

The regenerator was tested under different operating conditions in the cooling and the heat-pumping modes using distilled water as a heat transfer fluid. During all tests, the ambient temperature was maintained at  $25^{\circ}\text{C} \pm 1.5^{\circ}\text{C}$ . In the cooling mode, the HHEX temperature (i.e., the fluid inlet temperature on the hot side) was set at  $30^{\circ}\text{C}$ , whereas in the heat-pumping mode, the CHEX temperature (i.e., the fluid inlet temperature on the cold side) was set at  $20^{\circ}\text{C}$ . The constant inlet fluid temperatures were provided by a thermal bath that was hydraulically connected to the regenerator as discussed and shown schematically in [Figure S1](#) in the [supplemental information](#). In both operating modes, the regenerator was tested at different stress levels ( $\sigma$ ), different volume ratios ( $V^*$ ), and different operating frequencies ( $f$ ). Initially, stress levels between 620 and 825 MPa ( $\pm 10$  MPa) were applied at an operating frequency of 2 Hz and a displaced fluid volume ratio of 0.18 for the heat-pumping mode and 0.27 for the cooling mode (see [Figure 4E](#)). For all the tests, the lower stress limit at unloading was set at 20 MPa ( $\pm 10$  MPa). At stress levels of 775 and 825 MPa, the performance was further tested at three different operating frequencies (0.48, 0.9, and 2 Hz) and different values of the displaced fluid volume ratio and different cooling/heating powers. The applied elastocaloric regenerative cycle consists of four operating steps, namely mechanical loading and unloading and two fluid flow periods. The duration of loading and unloading periods were kept constant at 50 ms for all tests, and therefore, the operating frequency was changed only by the variation of the fluid flow periods, which were set at 1, 0.5, and 0.2 s, corresponding to the operating frequencies of 0.48, 0.9, and 2 Hz, respectively. It should be noted that during the fluid-flow periods, the strain of the regenerator was maintained constant in both loaded and unloaded positions. The displaced fluid volume ratio is defined as the ratio between the fluid volume in the (unloaded) regenerator ( $V_{0,\text{reg}}$ ) and the fluid volume displaced through the regenerator in a single fluid flow period ( $V_{\text{pump}}$ ):

$$V^* = \frac{V_{\text{pump}}}{V_{0,\text{reg}}} = \frac{\dot{m}_f \cdot P_f}{\rho_f \cdot V_{\text{reg}} \cdot \varepsilon} \quad (\text{Equation 1})$$

where  $\dot{m}_f$  is the mass-flow rate of the displaced fluid,  $P_f$  is the duration of the fluid-flow period,  $\rho_f$  is the density of the heat transfer fluid (i.e., distilled water) at the average operating temperature, whereas  $V_{\text{reg}}$  and  $\varepsilon$  are the volumes of the regenerator and its porosity, respectively. It should be noted that the mass-flow rate was not measured directly but calculated based on the piston displacement ( $\Delta l$ ), its cross-sectional area ( $A_{\text{piston}}$ ) and the duration of the blow period ( $P_f$ ):

$$\dot{m}_f = \frac{\Delta l \cdot A_{\text{piston}} \cdot \rho_f}{P_f} \quad (\text{Equation 2})$$

### Regenerator's performance metrics calculations

Under the steady-state conditions (i.e., when the regenerator's outlet temperatures are stable over time), the performance metrics of the elastocaloric regenerator were calculated. The temperature span is defined as the difference between the outlet temperature at the hot ( $T_{h,o}$ ) and cold ( $T_{c,o}$ ) sides of the regenerator averaged over 4 cycles after the steady-state conditions were reached:

$$T_{span} = \overline{T_{h,o}} - \overline{T_{c,o}}. \quad (\text{Equation 3})$$

The specific cooling and heating powers (per unit mass of the eCM in the regenerator) are defined as:

$$\dot{q}_c = \frac{\dot{Q}_c}{m_{eCM}} = \frac{\dot{m}_f \cdot c_{p,f} \cdot (\overline{T_{c,i}} - \overline{T_{c,o}})}{m_{eCM}}, \quad (\text{Equation 4a})$$

$$\dot{q}_h = \frac{\dot{Q}_h}{m_{eCM}} = \frac{\dot{m}_f \cdot c_{p,f} \cdot (\overline{T_{h,o}} - \overline{T_{h,i}})}{m_{eCM}}. \quad (\text{Equation 4b})$$

Where  $\dot{Q}_c$  and  $\dot{Q}_h$  are the absolute cooling and heating powers,  $m_{eCM}$  is the total mass of eCM in the regenerator (13.7 g),  $c_{p,f}$  is the specific heat of the heat transfer fluid (4,200 J/kgK), and  $T_{c,i}$ ,  $T_{c,o}$ ,  $T_{h,o}$  and  $T_{h,i}$  are the inlet temperature at the cold side, the outlet temperature at the cold side, the outlet temperature at the hot side, and the inlet temperature at the hot side, respectively.

The COP is defined as the ratio between the cooling/heating power and the input power, which includes the mechanical power ( $\dot{W}_{mech}$ ) required to load the regenerator and the power required to pump the fluid through the system ( $\dot{W}_{pump}$ ):

$$COP_{c(h)} = \frac{\dot{Q}_{c(h)}}{\dot{W}_{mech} + \dot{W}_{pump}}. \quad (\text{Equation 5})$$

The mechanical input power, assuming a perfect work recovery upon unloading as discussed in the [results and discussion](#) section, corresponds to the area enclosed in the stress ( $\sigma$ )-strain ( $\epsilon$ ) diagram ( $\oint \sigma d\epsilon$ ), as shown for example in [Figure 6F](#) and is calculated as follows:

$$\dot{W}_{mech} = f \cdot V_{eCM} \oint \sigma d\epsilon. \quad (\text{Equation 6})$$

where  $f$  is the operating frequency and  $V_{eCM}$  is the volume of eCM in the regenerator.

The power required to pump the fluid is calculated based on the pressure drop measurements (see [Note S6](#) and [Figure S8](#) in the [supplemental information](#)) and is calculated as follows:

$$\dot{W}_{pump} = \frac{\dot{m}_f \cdot \overline{\Delta p}}{\rho_f}. \quad (\text{Equation 7})$$

Finally, the exergy efficiency (also called the second law efficiency) is defined as the ratio between the actual COP values (Equation 5) and the maximum possible COP value at a given temperature span (Carnot COP) and is calculated as:

$$\zeta_{c(h)} = \frac{COP_{c(h)}}{COP_{Car,c(h)}} = \frac{COP_{c(h)}}{\frac{\overline{T_{c(i,o)}}}{\overline{T_{h,o}} - \overline{T_{c,o}}}}. \quad (\text{Equation 8})$$

## SUPPLEMENTAL INFORMATION

Supplemental information can be found online at <https://doi.org/10.1016/j.joule.2022.08.011>.

## ACKNOWLEDGMENTS

This work was supported by the European Research Council under the Horizon 2020 program (ERC starting grant no. 803669). Jaka Tušek would also like to acknowledge the support of the Slovenian Research Agency (Core funding no. P2-0422).

## AUTHOR CONTRIBUTIONS

Conceptualization, Ž.A., S.D., A.Ž., M.B., J.K., and J.T.; methodology, Ž.A., S.D., U.Ž.B., S.Z., and J.T.; software, Ž.A., S.D., and U.Ž.B.; validation, Ž.A. and S.D.; formal analysis, Ž.A.; investigation, Ž.A., S.D., L.P., P.K., and J.C.; resources, J.T.; writing – original draft, Ž.A., S.D., and J.T.; writing – review & editing, Ž.A., S.D., A.Ž., U.Ž.B., L.P., P.K., J.C., S.Z., M.B., J.K., and J.T.; visualization, Ž.A. and J.T.; supervision, M.B., J.K., and J.T.; funding acquisition, J.T.

## DECLARATION OF INTERESTS

The authors declare no competing interests.

Received: June 11, 2022

Revised: July 19, 2022

Accepted: August 22, 2022

Published: September 20, 2022

## REFERENCES

1. Coulomb, D., Dupont, J.-L., and Marlet, V. (2017). The Impact of the Refrigeration Sector on Climate Change, 35th Informatory Note on Refrigeration Technologies.
2. Isaac, M., and van Vuuren, D.P. (2009). Modeling global residential sector energy demand for heating and air conditioning in the context of climate change. *Energy Policy* 37, 507–521. <https://doi.org/10.1016/j.enpol.2008.09.051>.
3. Steven Brown, J., and Domanski, P.A. (2014). Review of alternative cooling technologies. *Appl. Therm. Eng.* 64, 252–262. <https://doi.org/10.1016/j.applthermaleng.2013.12.014>.
4. Goetzler, W., Zogg, R., Young, J., and Johnson, C. (2014). Energy savings potential and RD & D opportunities for Non-vapor-compression HVAC technologies. US Dep. Energy 3673. <https://doi.org/10.2172/1220817>.
5. IEA. Average efficiency of new air conditioners 2000–2020 and in the Net Zero Scenario (IEA). <https://www.iea.org/data-and-statistics/charts/average-efficiency-of-new-air-conditioners-2000-2020-and-in-the-net-zero-scenario>.
6. Kitanovski, A. (2020). Energy applications of magnetocaloric materials. *Adv. Energy Mater.* 10, 1903741. <https://doi.org/10.1002/aenm.201903741>.
7. Kauffeld, M. (2016). 31st Informatory Note on Refrigeration Technologies. *Current Long-Term Alternative Refrigerants and Their Applications*.
8. Secretariat, Ozone (2020). Handbook for the Montreal Protocol on Substances that Deplete the Ozone Layer.
9. Fähler, S., and Pecharsky, V.K. (2018). Caloric effects in ferroic materials. *MRS Bull* 43, 264–268. <https://doi.org/10.1557/mrs.2018.66>.
10. Moya, X., and Mathur, N.D. (2020). Caloric materials for cooling and heating. *Science* 370, 797–803. <https://doi.org/10.1126/science.abb0973>.
11. Hou, H., Qian, S., and Takeuchi, I. (2022). Materials, physics and systems for multicaloric cooling. *Nat. Rev. Mater.* 7, 633–652. <https://doi.org/10.1038/s41578-022-00428-x>.
12. Shi, J., Han, D., Li, Z., Yang, L., Lu, S.G., Zhong, Z., Chen, J., Zhang, Q.M., and Qian, X. (2019). Electrocaloric cooling materials and devices for zero-global-warming-potential, high-efficiency refrigeration. *Joule* 3, 1200–1225. <https://doi.org/10.1016/j.joule.2019.03.021>.
13. Lloveras, P., and Tamarit, J.-L. (2021). Advances and obstacles in pressure-driven solid-state cooling: a review of barocaloric materials. *MRS Energy Sustain* 8, 3–15. <https://doi.org/10.1557/s43581-020-00002-4>.
14. Kitanovski, A., Tušek, J., Tomc, U., Plaznik, U., Ožbolt, M., and Poredoš, A. (2015). *Magnetocaloric Energy Conversion—From Theory to Applications* (Springer).
15. Greco, A., Aprea, C., Maiorino, A., and Masselli, C. (2019). A review of the state of the art of solid-state caloric cooling processes at room-temperature before 2019. *Int. J. Refrig.* 106, 66–88. <https://doi.org/10.1016/j.ijrefrig.2019.06.034>.
16. Masche, M., Liang, J., Engelbrecht, K., and Bahl, C.R.H. (2022). Performance assessment of a rotary active magnetic regenerator prototype using gadolinium. *Appl. Therm. Eng.* 204, 117947. <https://doi.org/10.1016/j.applthermaleng.2021.117947>.
17. VHK and armines (2016). Technology Roadmap in Preparatory/Review Study on Commission Regulation (EC) No. 643/2009 with Regard to Ecodesign Requirements for Household Refrigeration Appliances and Commission Delegated Regulation (EU).
18. Cui, J., Wu, Y., Muehlbauer, J., Hwang, Y., Radermacher, R., Fackler, S., Wuttig, M., and Takeuchi, I. (2012). Demonstration of high efficiency elastocaloric cooling with large  $\Delta T$  using NiTi wires. *Appl. Phys. Lett.* 101, 73904. <https://doi.org/10.1063/1.4746257>.
19. Ossmer, H., Lambrecht, F., Gültig, M., Chluba, C., Quandt, E., and Kohl, M. (2014). Evolution of temperature profiles in TiNi films for elastocaloric cooling. *Acta Mater* 81, 9–20. <https://doi.org/10.1016/j.actamat.2014.08.006>.
20. Tušek, J., Engelbrecht, K., Mikkelsen, L.P., and Pryds, N. (2015). Elastocaloric effect of Ni-Ti wire for application in a cooling device. *J. Appl. Phys.* 117. <https://doi.org/10.1063/1.4913878>.
21. Porenta, L., Kabirifar, P., Žerovnik, A., Čebren, M., Žužek, B., Dolenc, M., Brojan, M., and Tušek, J. (2020). Thin-walled Ni-Ti tubes under

- compression: ideal candidates for efficient and fatigue-resistant elastocaloric cooling. *Appl. Mater. Today* 20, 100712. <https://doi.org/10.1016/j.apmt.2020.100712>.
22. Chluba, C., Ge, W., Lima de Miranda, R.L., Strobel, J., Kienle, L., Quandt, E., and Wuttig, M. (2015). Shape memory alloys. Ultralow-fatigue shape memory alloy films. *Science* 348, 1004–1007. <https://doi.org/10.1126/science.1261164>.
  23. Chluba, C., Ossmer, H., Zamponi, C., Kohl, M., and Quandt, E. (2016). Ultra-low fatigue quaternary TiNi-based films for elastocaloric cooling. *Shape Mem. Superelasticity* 2, 95–103. <https://doi.org/10.1007/s40830-016-0054-3>.
  24. Schmidt, M., Ullrich, J., Wieczorek, A., Frenzel, J., Schütze, A., Eggeler, G., and Seelecke, S. (2015). Thermal stabilization of NiTiCuV shape memory alloys: observations During elastocaloric training. *Shape Mem. Superelasticity* 1, 132–141. <https://doi.org/10.1007/s40830-015-0021-4>.
  25. Yang, Z., Cong, D., Yuan, Y., Li, R., Zheng, H., Sun, X., Nie, Z., Ren, Y., and Wang, Y. (2020). Large room-temperature elastocaloric effect in a bulk polycrystalline Ni-Ti-Cu-Co alloy with low isothermal stress hysteresis. *Appl. Mater. Today* 21, 100844. <https://doi.org/10.1016/j.apmt.2020.100844>.
  26. Mañosa, L., Jarque-Farnos, S., Vives, E., and Planes, A. (2013). Large temperature span and giant refrigerant capacity in elastocaloric Cu-Zn-Al shape memory alloys. *Appl. Phys. Lett.* 103, 211904. <https://doi.org/10.1063/1.4832339>.
  27. Qian, S., Geng, Y., Wang, Y., Pillsbury, T.E., Hada, Y., Yamaguchi, Y., Fujimoto, K., Hwang, Y., Radermacher, R., Cui, J., et al. (2016). Elastocaloric effect in CuAlZn and CuAlMn shape memory alloys under compression. *Philos. Trans. A Math. Phys. Eng. Sci.* 374, 20150309. <https://doi.org/10.1098/rsta.2015.0309>.
  28. Xiao, F., Bucsek, A., Jin, X., Porta, M., and Planes, A. (2022). Giant elastic response and ultra-stable elastocaloric effect in twinned textured Fe-Pd single crystals. *Acta Mater* 223, 117486. <https://doi.org/10.1016/j.actamat.2021.117486>.
  29. Liu, J., Zhao, D., and Li, Y. (2017). Exploring magnetic elastocaloric materials for solid-state cooling. *Shape Mem. Superelasticity* 3, 192–198. <https://doi.org/10.1007/s40830-017-0118-z>.
  30. Tong, W., Liang, L., Xu, J., Wang, H.J., Tian, J., and Peng, L.M. (2022). Achieving enhanced mechanical, pseudoelastic and elastocaloric properties in Ni-Mn-Ga alloys via Dy micro-alloying and isothermal mechanical cyclic training. *Scr. Mater.* 209, 114393. <https://doi.org/10.1016/j.scriptamat.2021.114393>.
  31. Zhang, S., Yang, Q., Li, C., Fu, Y., Zhang, H., Ye, Z., Zhou, X., Li, Q., Wang, T., Wang, S., et al. (2022). Solid-state cooling by elastocaloric polymer with uniform chain-lengths. *Nat. Commun.* 13, 9. <https://doi.org/10.1038/s41467-021-27746-y>.
  32. Bennacer, R., Liu, B., Yang, M., and Chen, A. (2022). Refrigeration performance and the elastocaloric effect in natural and synthetic rubbers. *Appl. Therm. Eng.* 204, 117938. <https://doi.org/10.1016/j.applthermaleng.2021.117938>.
  33. Cong, D., Xiong, W., Planes, A., Ren, Y., Mañosa, L., Cao, P., Nie, Z., Sun, X., Yang, Z., Hong, X., et al. (2019). Colossal elastocaloric effect in ferroelastic Ni-Mn-Ti alloys. *Phys. Rev. Lett.* 122, 255703. <https://doi.org/10.1103/PhysRevLett.122.255703>.
  34. Kabirifar, P., Žerovnik, A., Ahčin, Ž., Porenta, L., Brojan, M., and Tušek, J. (2019). Elastocaloric cooling: state-of-the-art and future challenges in designing regenerative elastocaloric devices. *J. Mech. Eng.* 65, 615–630. <https://doi.org/10.5545/sv-jme.2019.6369>.
  35. Imran, M., and Zhang, X. (2020). Recent developments on the cyclic stability in elastocaloric materials. *Mater. Des.* 195, 109030. <https://doi.org/10.1016/j.matdes.2020.109030>.
  36. Zhang, J., Xu, Y., An, S., Sun, Y., Li, X., and Li, Y. (2020). Giant mechanocaloric materials for solid-state cooling. *Chin. Phys. B* 29, 76202. <https://doi.org/10.1088/1674-1056/ab8a40>.
  37. Chen, J., Lei, L., and Fang, G. (2021). Elastocaloric cooling of shape memory alloys: a review. *Mater. Today Commun.* 28, 102706. <https://doi.org/10.1016/j.mtcomm.2021.102706>.
  38. Imran, M., and Zhang, X. (2021). Reduced dimensions elastocaloric materials: A route towards miniaturized refrigeration. *Mater. Des.* 206, 109784. <https://doi.org/10.1016/j.matdes.2021.109784>.
  39. Schmidt, M., Schütze, A., and Seelecke, S. (2015). Scientific test setup for investigation of shape memory alloy based elastocaloric cooling processes. *Int. J. Refrig.* 54, 88–97. <https://doi.org/10.1016/j.ijrefrig.2015.03.001>.
  40. Bruederlin, F., Bumke, L., Ossmer, H., Chluba, C., Quandt, E., and Kohl, M. (2018). Elastocaloric cooling on the miniature scale: a review on materials and engineering of devices. *Energy Technol* 6, 1588–1604. <https://doi.org/10.1002/ente.201800137>.
  41. Ulpiani, G., Bruederlin, F., Weidemann, R., Ranzi, G., Santamouris, M., and Kohl, M. (2020). Upscaling of SMA film-based elastocaloric cooling. *Appl. Therm. Eng.* 180, 115867. <https://doi.org/10.1016/j.applthermaleng.2020.115867>.
  42. Greibich, F., Schwödau, R., Mao, G., Wirthl, D., Drack, M., Baumgartner, R., Kogler, A., Stadlbauer, J., Bauer, S., Arnold, N., et al. (2021). Elastocaloric heat pump with specific cooling power of 20.9 W g<sup>-1</sup> exploiting snap-through instability and strain-induced crystallization. *Nat. Energy* 6, 260–267. <https://doi.org/10.1038/s41560-020-00770-w>.
  43. Chen, Y., Wang, Y., Sun, W., Qian, S., and Liu, J. (2022). A compact elastocaloric refrigerator. *Innovation (Camb)* 3, 100205. <https://doi.org/10.1016/j.xinn.2022.100205>.
  44. Qian, S., Geng, Y., Wang, Y., Muehlbauer, J., Ling, J., Hwang, Y., Radermacher, R., and Takeuchi, I. (2016). Design of a hydraulically driven compressive elastocaloric cooling system. *Sci. Technol. Built Environ.* 22, 500–506. <https://doi.org/10.1080/23744731.2016.1171630>.
  45. Qian, S., Wu, Y., Ling, J., Muehlbauer, J., Hwang, Y., Takeuchi, I., and Radermacher, R. (2015). Design, development and testing of a compressive thermoelastic cooling prototype. *Proceedings of the 24th IIR International Congress of Refrigeration*.
  46. Tušek, J., Engelbrecht, K., Eriksen, D., Dall'Olio, S., Tušek, J., and Pryds, N. (2016). A regenerative elastocaloric heat pump. *Nat. Energy* 1, 1–6. <https://doi.org/10.1038/energy.2016.134>.
  47. Engelbrecht, K., Tušek, J., Eriksen, D., Lei, T., Lee, C.Y., Tušek, J., and Pryds, N. (2017). A regenerative elastocaloric device: experimental results. *J. Phys. D: Appl. Phys.* 50. <https://doi.org/10.1088/1361-6463/aa8656>.
  48. Kirsch, S.M., Welsch, F., Michaelis, N., Schmidt, M., Wieczorek, A., Frenzel, J., Eggeler, G., Schütze, A., and Seelecke, S. (2018). NiTi-based elastocaloric cooling on the macroscale: From basic concepts to realization. *Energy Technol* 6, 1567–1587. <https://doi.org/10.1002/ente.201800152>.
  49. Snodgrass, R., and Erickson, D. (2019). A multistage elastocaloric refrigerator and heat pump with 28 K temperature span. *Sci. Rep.* 9, 18532. <https://doi.org/10.1038/s41598-019-54411-8>.
  50. Ianniciello, L., Bartholomé, K., Fitger, A., and Engelbrecht, K. (2022). Long life elastocaloric regenerator operating under compression. *Appl. Therm. Eng.* 202, 117838. <https://doi.org/10.1016/j.applthermaleng.2021.117838>.
  51. Bachmann, N., Fitger, A., Maier, L.M., Mahlke, A., Schäfer-Welsen, O., Koch, T., and Bartholomé, K. (2021). Long-term stable compressive elastocaloric cooling system with latent heat transfer. *Commun. Phys.* 4, 194. <https://doi.org/10.1038/s42005-021-00697-y>.
  52. Catalini, D. (2021). Development of cooling systems with active elastocaloric regenerators. *PhD Thesis (University of Maryland)*.
  53. Zhang, J., Zhu, Y., Cheng, S., Yao, S., and Sun, Q. (2022). Enhancing cooling performance of NiTi elastocaloric tube refrigerant via internal grooving. *Appl. Therm. Eng.* 213, 118657. <https://doi.org/10.1016/j.applthermaleng.2022.118657>.
  54. Hou, H., Cui, J., Qian, S., Catalini, D., Hwang, Y., Radermacher, R., and Takeuchi, I. (2018). Overcoming fatigue through compression for advanced elastocaloric cooling. *MRS Bull* 43, 285–290. <https://doi.org/10.1557/mrs.2018.70>.
  55. Liang, D., Wang, Q., Chu, K., Chen, J., Hua, P., Ren, F., and Sun, Q. (2022). Ultrahigh cycle fatigue of nanocrystalline NiTi tubes for elastocaloric cooling. *Appl. Mater. Today* 26, 101377. <https://doi.org/10.1016/j.apmt.2022.101377>.
  56. Chen, J., Zhang, K., Kan, Q., Yin, H., and Sun, Q. (2019). Ultra-high fatigue life of NiTi cylinders for compression-based elastocaloric cooling. *Appl. Phys. Lett.* 115, 93902. <https://doi.org/10.1063/1.5115793>.
  57. Zhang, K., Kang, G., and Sun, Q. (2019). High fatigue life and cooling efficiency of NiTi shape memory alloy under cyclic compression. *Scr. Mater.* 159, 62–67. <https://doi.org/10.1016/j.scriptamat.2018.09.012>.

58. Tušek, J., Engelbrecht, K., Millán-Solsona, R., Mañosa, L., Vives, E., Mikkelsen, L.P., and Pryds, N. (2015). The elastocaloric effect: a way to cool efficiently. *Adv. Energy Mater.* 5, 1500361. <https://doi.org/10.1002/aenm.201500361>.
59. Meng, Y., Pu, J., and Pei, Q. (2021). Electrocaloric cooling over high device temperature span. *Joule* 5, 780–793. <https://doi.org/10.1016/j.joule.2020.12.018>.
60. Ahčin, Ž., Liang, J., Engelbrecht, K., and Tušek, J. (2021). Thermo-hydraulic evaluation of oscillating-flow shell-and-tube-like regenerators for (elasto)caloric cooling. *Appl. Therm. Eng.* 190, 116842. <https://doi.org/10.1016/j.applthermaleng.2021.116842>.
61. Frenzel, J., George, E.P., Dlouhy, A., Somsen, C., Wagner, M.F.-X., and Eggeler, G. (2010). Influence of Ni on martensitic phase transformations in NiTi shape memory alloys. *Acta Mater* 58, 3444–3458. <https://doi.org/10.1016/j.actamat.2010.02.019>.
62. Torelló, À., and Defay, E. (2021). Heat exchange law in caloric regenerators. *Int. J. Refrig.* 127, 174–179. <https://doi.org/10.1016/j.ijrefrig.2021.02.024>.
63. Frenzel, J., Wiczorek, A., Opahle, I., Maaß, B., Drautz, R., and Eggeler, G. (2015). On the effect of alloy composition on martensite start temperatures and latent heats in Ni–Ti-based shape memory alloys. *Acta Mater* 90, 213–231. <https://doi.org/10.1016/j.actamat.2015.02.029>.
64. Jacobs, S., Auringer, J., Boeder, A., Chell, J., Komorowski, L., Leonard, J., Russek, S., and Zimm, C. (2014). The performance of a large-scale rotary magnetic refrigerator. *Int. J. Refrig.* 37, 84–91. <https://doi.org/10.1016/j.ijrefrig.2013.09.025>.
65. Rowe, A., and Tura, A. (2006). Experimental investigation of a three-material layered active magnetic regenerator. *Int. J. Refrig.* 29, 1286–1293. <https://doi.org/10.1016/j.ijrefrig.2006.07.012>.
66. Engelbrecht, K., Eriksen, D., Bahl, C.R.H., Bjørk, R., Geyti, J., Lozano, J.A., Nielsen, K.K., Saxild, F., Smith, A., and Pryds, N. (2012). Experimental results for a novel rotary active magnetic regenerator. *Int. J. Refrig.* 35, 1498–1505. <https://doi.org/10.1016/j.ijrefrig.2012.05.003>.
67. Lionte, S., Risser, M., and Muller, C. (2021). A 15kW magnetocaloric proof-of-concept unit: initial development and first experimental results. *Int. J. Refrig.* 122, 256–265. <https://doi.org/10.1016/j.ijrefrig.2020.09.019>.
68. Tura, A., and Rowe, A. (2011). Permanent magnet magnetic refrigerator design and experimental characterization. *Int. J. Refrig.* 34, 628–639. <https://doi.org/10.1016/j.ijrefrig.2010.12.009>.
69. Ma, R., Zhang, Z., Tong, K., Huber, D., Kornbluh, R., Ju, Y.S., and Pei, Q. (2017). Highly efficient electrocaloric cooling with electrostatic actuation. *Science* 357, 1130–1134. <https://doi.org/10.1126/science.aan5980>.
70. Plaznik, U., Vrabelj, M., Kutnjak, Z., Malič, B., Rožič, B., Poredoš, A., and Kitanovski, A. (2019). Numerical modelling and experimental validation of a regenerative electrocaloric cooler. *Int. J. Refrig.* 98, 139–149. <https://doi.org/10.1016/j.ijrefrig.2018.10.029>.
71. Meng, Y., Zhang, Z., Wu, H., Wu, R., Wu, J., Wang, H., and Pei, Q. (2020). A cascade electrocaloric cooling device for large temperature lift. *Nat. Energy* 5, 996–1002. <https://doi.org/10.1038/s41560-020-00715-3>.
72. Torelló, À., Lheritier, P., Usui, T., Nouchokgwe, Y., Gérard, M., Bouton, O., Hirose, S., and Defay, E. (2020). Giant temperature span in electrocaloric regenerator. *Science* 370, 125–129. <https://doi.org/10.1126/science.abb8045>.
73. Wang, Y., Zhang, Z., Usui, T., Benedict, M., Hirose, S., Lee, J., Kalb, J., and Schwartz, D. (2020). A high-performance solid-state electrocaloric cooling system. *Science* 370, 129–133. <https://doi.org/10.1126/science.aba2648>.
74. Qian, S., Wang, Y., Geng, Y., Ling, J., Muehlbauer, J., Hwang, Y., Radermacher, R., and Takeuchi, I. (2016). Experimental evaluation of a compressive elastocaloric cooling system. 16th International Refrigeration and Air Conditioning Conference at Purdue 2385, 16.
75. Qian, S., Geng, Y., Wang, Y., Ling, J., Hwang, Y., Radermacher, R., Takeuchi, I., and Cui, J. (2016). A review of elastocaloric cooling: materials, cycles and system integrations. *Int. J. Refrig.* 64, 1–19. <https://doi.org/10.1016/j.ijrefrig.2015.12.001>.
76. Slaughter, J., Czernuszewicz, A., Griffith, L., and Pecharsky, V. (2020). Compact and efficient elastocaloric heat pumps - Is there a path forward? *J. Appl. Phys.* 127, 194501. <https://doi.org/10.1063/5.0003275>.
77. Žkauskas, A. (1987). Heat transfer from tubes in crossflow. *Adv. Heat Transf.* 18, 87–159. [https://doi.org/10.1016/S0065-2717\(08\)70118-7](https://doi.org/10.1016/S0065-2717(08)70118-7).